ENGINEERING

An energy-embodied paralleled liquid manipulation for equipment-free, quantitative multiplexed liver function monitoring

Chao Liang[1], Jingyang Zhao[1], Pingdong Wei[1], Kang Wei[2], Hanqing Jiang[1,3,4]*

Comprehensive liver function monitoring is vital for liver damage diagnoses. However, multiplexed testing with clinical accuracy often requires paralleled liquid manipulation to avoid reagent interference and nonspecific adsorption, making it restricted to centralized facilities and specialists. Here, we report an equipment-free, quantitative, and multiplexed point-of-care testing (POCT), the energy-embodied POCT (EE-POCT). The driving energy (pressured gas) and liquid reagents are embodied in separate rigid-flexible chambers through a mechanical pressure sensing mechanism to achieve a paralleled, interference-free, and multiple-reagent operation with no need for external equipment. The EE-POCT achieves quantitative results for nine liver-related indicators from 180 microliters of whole blood within 4 minutes. Validated with 103 clinical specimens, it shows high concordance with a clinical gold standard analyzer (Pearson coefficients >0.9). The EE-POCT platform not only advances liver health diagnostics but also sets a precedent for developing versatile, accessible medical technologies that can significantly affect global health outcomes.

INTRODUCTION

Liver, the largest solid organ in the body, is crucial for metabolism and detoxification (*1*). Increasing consumption of sugar, alcohol, and medication has led to a rise in liver-related conditions such as nonalcoholic fatty liver disease (NAFLD)—affecting 17 to 51% of adults (*2*)—nonalcoholic steatohepatitis (NASH), and cirrhosis. The COVID-19 pandemic has further exacerbated these injuries, mainly due to certain medications used during hospitalization, highlighting the need for frequent monitoring and evaluation (*3*, *4*). Liver disease accounts for more than 2 million deaths annually (cirrhosis, viral hepatitis, and liver cancer) and accounts for 4% of all deaths worldwide (*5*), with projections indicating a 56% increase in NASH-associated cirrhosis and a 77% increase in alcohol-associated cirrhosis in the US by 2040 (*6*). However, traditional diagnostics often rely on a limited set of biomarkers such as alanine aminotransferase (ALT) and aspartate aminotransferase (AST) (*7*, *8*), which may fail to provide accurate diagnoses. For example, ALT and AST levels may remain within the normal clinical range (NCR) or become slightly elevated in both mild NAFLD and serious cirrhosis, but cirrhosis often demonstrates a decrease in the level of proteins (*9*, *10*) (Fig. 1A). Thus, a comprehensive liver function test, including markers such as AST, ALT, alkaline phosphatase (ALP), total protein (TP), albumin (ALB), globin (GLB), and electrolyte, is crucial for effective monitoring and prevention of progression from mild NAFLD to severe cirrhosis or liver cancer (Fig. 1A). However, these tests are typically confined to centralized laboratories, requiring professional handling, making them costly and inaccessible in resource-limited areas (*11*). There is a pressing need for an affordable, user-friendly, and equipment-free system capable of quantitative and multiplexed point-of-care testing (POCT) for essential liver biomarkers.

Current clinical testing strategies for liver function biomarker primarily rely on electrochemical (*12*), optical (*13*), and colorimetric (*14*) methods. Among these, the colorimetric method is particularly well suited for multiplexed POCT. On one hand, colorimetric reactions are available for all major liver-related biomarkers and can be easily integrated into a single, low-cost device. On the other hand, results can be visually interpreted by the naked eye or captured through smartphone cameras (*15*), thus eliminating the need for additional equipment such as lenses, batteries, or circuit boards. However, achieving reliable quantitative colorimetric detection remains a challenge. Variation in color accuracy due to different lighting conditions or camera types can affect results. One promising solution to address this issue involves applying machine learning algorithms to calibrate and predict true color (*16*, *17*). This approach, however, requires extensive training data across varied sample concentrations and light conditions to ensure precision. Such a setup is labor intensive and any alternation in reagent formulations or camera specifications necessities another round of machining learning process.

For multiplexed POCT with clinical accuracy, paralleled reagent manipulation where different biomarkers are tested in separate chambers is often required to avoid unintended reagent interference and nonspecific adsorption. However, most existing multiplexed POCT devices generally fail to simultaneously achieve paralleled liquid manipulation, clinical accuracy, equipment-free, and ease of use (Fig. 1B). For example, lateral flow strips (LFS) or paper-based microfluidics (μPAD) (*18*–*20*) offer low cost and ease of use, but the residual detectable complex from the pores of chromatographic membranes may result in nonspecific adsorption, decline of the detection signal, and increase in the background noise, limiting them to qualitative single biomarker detections (*21*–*23*). Capillary-driven and gravity-driven microfluidic chips (often called passive microfluidics) have uniform sample flow behavior in the silicon- or polymer-based microchannels (*24*–*26*), but like LFS, the residuals in the channel from their sequential chain reaction may also cause reagent interference and nonspecific adsorption issues. Moreover, because the capillary flow is generated at the liquid-air interface, no additional flows can be introduced once the channels are filled, making

[1]School of Engineering, Westlake University, Hangzhou, Zhejiang 310030, China. [2]Westlake Interactive Robot Technology (Hangzhou) Co. Ltd., Hangzhou, Zhejiang 310000, China. [3]Research Center for Industries of the Future, Westlake University, Hangzhou, Zhejiang 310030, China. [4]Westlake Institute for Advanced Study, Hangzhou, Zhejiang 310024, China.
*Corresponding author. Email: hanqing.jiang@westlake.edu.cn

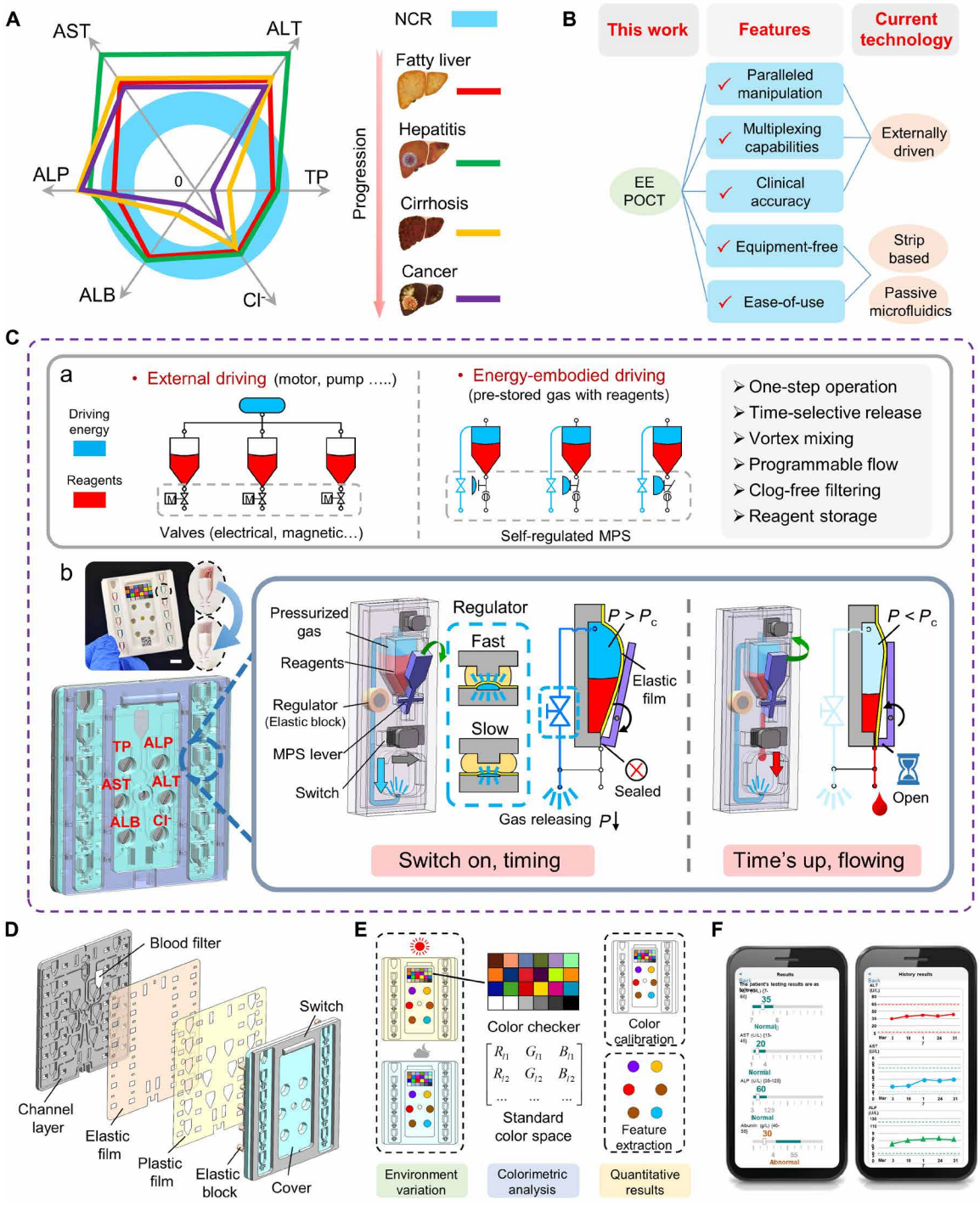

Fig. 1. Energy-embodied point-of-care test (EE-POCT). (**A**) A combination of biomarkers can comprehensively reflect the liver conditions from mild fatty liver to severe cirrhosis. NCR indicates normal clinical range. (**B**) Features of the EE-POCT compared with current POCT technologies. (**C**) Mechanism of the energy-embodied microfluidics. (a) Comparison of paralleled manipulation for the external driving and energy-embodied driving. (b) Schematic view of the EE-POCT technology. The inset is a picture of the EE-POCT platform with a scale bar of 6 mm. (**D**) Expanded view schematic diagram of the EE-POCT platform. (**E**) Colorimetric analysis algorithm. (**F**) Custom mobile application for quantitative liver function monitoring.

multibiomarker assays cumbersome and dependent on multiple sample-loading steps (*27*). Pneumatic-driven devices can support parallel reagent manipulation, but they require external air pumps (positive or negative), making them bulky, expensive, and unsuitable for low-resource environments (*28*–*30*). Manual pressure-driven devices offer a pump-free alternative by using mechanical buttons (*31*–*33*), but user-dependent variability and the lack of automated timing control pose challenges, particularly for assays involving multiple reagents.

In this paper, we report an energy-embodied POCT testing (EE-POCT) technology that achieves autonomous paralleled liquid manipulation without the need of external power, by integrating the driving and manipulation energy (pressurized gas) and liquid reagents within a specific rigid-flexible compound chamber (Fig. 1C). This platform has the merits of both passive microfluidics and externally powered devices. On one hand, the EE-POCT operates through our proposed mechanical pressure sensing (MPS), achieving paralleled manipulation of reagents, such as independently time-selective releasing, programmable flowing, vortex mixing, and clog-free blood filtering. In this case, different reagents are capable of reacting in separate chambers for different biomarkers, avoiding the nonspecific and reagent interference issues and achieving clinically applicable accuracy. On the other hand, this platform is free of equipment due to the embodied driving and manipulation energy, and only consisted of several rigid and flexible layers (Fig. 1D) that can be readily mass manufactured by using three-dimensional (3D) printing or mold injection technology, making it cost-effective (about $0.40 see table S2). Further achieving the device's equipment-free signature, we use a smartphone-based colorimetric analysis algorithm (Fig. 1, E and F) that uses a color checker with a standard color space to ensure accurate color readings under various lighting conditions. This approach eliminates the need for extensive machine learning training, streaming the operation. Our EE-POCT platform can quantitatively measure nine critical liver-related indicators (AST, ALT, ALP, TP, ALB, GLB, Cl^-, AST/ALT ratio, and ALB/GLB ratio) from just 180 μl of whole blood in under 4 min. Validation against 103 clinical specimens has shown good concordance with a clinical gold standard analyzer, with Pearson coefficients exceeding 0.9. Compared to the current POCT technologies (table S1), our EE-POCT platform offers high accurate quantitative results, multiplexing capabilities (supporting the largest number of analytes among existing technologies), good affordability (offering the lowest cost per biomarker), and high efficiency (delivering the fastest processing speeds compared to alternatives). We also tested the specimens from 36 diagnosed patients with fatty liver, hepatitis, cirrhosis, and liver cancer using the EE-POCT platform to assess the correlation between the liver biomarkers and the liver diseases. This technology fulfills all WHO's ASSURED criteria (Affordable, Sensitive, Specific, User-friendly, Rapid and robust, Equipment-free, and Deliverable to the end users) (*34*), pointing to notable potential for broadening the accessibility and efficacy of liver health diagnostics in a variety of settings, particularly in resource-limited areas. The EE-POCT not only meets but advances the global standards for point-of-care diagnostics, presenting a substantial step forward in accessible medical testing.

RESULTS

Colorimetric assay and evaluation

Various colorimetric assays were developed and optimized, focusing on refining the reaction steps and curing times to enable simultaneous multiplexed assays within an integrated EE-POCT platform. Colorimetric assays were selected due to their rapid response, ease of use, and compatibility with visual and automated analysis, making them ideally suited for POCT diagnostics. These assays are particularly effective in monitoring liver function, as the liver synthesizes key proteins such as ALB and GLB. Changes in the levels of these proteins can indicate liver dysfunction, which may manifest clinically as symptoms like edema and ascites (*35*). By accurately and rapidly detecting these protein levels, colorimetric assays provide crucial data for assessing liver health and guiding treatment decisions.

Figure 2 illustrates the materials and characterizations of the colorimetric assays used to monitor liver functions. Specifically, ALB binds with the reagent Bromo-cresol green, inducing a color change from yellow to green (Fig. 2A). The ultraviolet-visible (UV-vis) absorbance (Shimadzu, UV3600 Plus) was recorded immediately and up to 3 min postreagent addition, showing that the absorbance almost remained consistent over the varied reaction times (Fig. 2B). The ALB assay exhibited a linear relationship across the concentration range of 10 to 80 g/liter at 630 nm, with an R^2 value of 0.97 (Fig. 2C), indicating robust assay performance within the NCR for ALB, which is 35 to 50 g/liter.

The TP concentration in blood is determined using the biuret method, where the polypeptide in proteins coordinate with Cu^{2+} under alkaline conditions, forming a purple color complex (Fig. 2D). UV-vis absorbance measurements indicate strong linearity with an R^2 value of 0.99 at 540 nm over a reaction of 3 min (Fig. 2, E and F). The assay's tested concentration range of 20 to 100 g/liter covers the NCR of 65 to 85 g/liter. It is noted that GLB concentrations can be indirectly obtained by subtracting the ALB concentrations from the TP measurements.

Electrolyte disturbances are common in the liver disease such as cirrhosis, often resulting in lower concentrations of K^+, Na^+, and Cl^- in the blood due to the multiple opposing factors affecting fluid homeostasis (*36*). The assay for Cl^- uses mercuric thiocyanate, reacting with Cl^- to produce SCN^-, which subsequently reacts with Fe^{3+}, forming an orange-colored product (Fig. 2G). UV-vis absorbance measurements, taken 3 min postreagent addition, show minimal variation (Fig. 2H). The assay's linearity was excellent, with an R^2 value of 0.98 at 450 nm (Fig. 2I), covering a concentration range of 50 to 125 mM, which encompasses the NCR of 99 to 100 mM.

ALP, widely distributed in the liver, bone, and kidney, serves as an indicator of liver disease, particularly signaling biliary obstruction and jaundice (*37*). The ALP assay uses disodium phenyl phosphate (DPP) as an artificial substrate. Under the catalysis of ALP, DPP is decomposed into phenol and disodium hydrogen phosphate. In an alkaline environment, phenol reacts with 4-aminoantipyrine by the oxidation of potassium ferricyanide (PF), forming a red-colored product (Fig. 2J). The assay exhibited an R^2 value of 0.97 at 520 nm (Fig. 2L) when the mixture of 4-aminoantipyrine, phenol, and OH^- was immediately added after introducing the substrate DPP. Delay in adding this mixture led to saturation at high ALP concentrations, which could not be distinguished by UV-vis absorbance (Fig. 2K). The test covered an ALP concentration range of 10 to 150 U/liter, aligning with the NCR for adults of 50 to 135 U/liter.

Transaminases, mainly existing in liver, are the most frequently used and specific indicators of liver injury. When liver cells are damaged, transaminases such as AST and ALT are released into the bloodstream, leading to an increase in their concentrations (*38*).

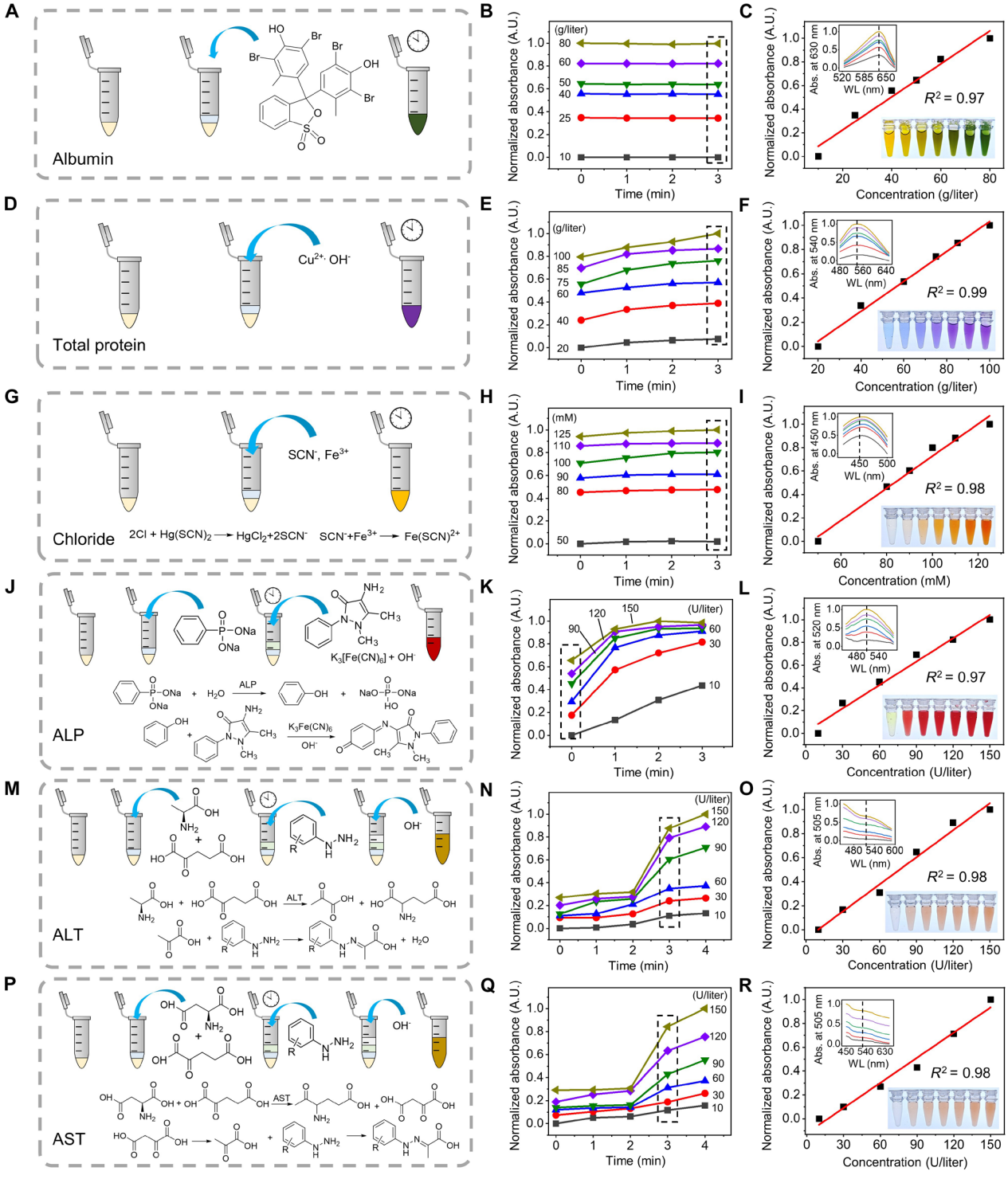

Fig. 2. Materials and characterization for the colorimetric assay. (**A**, **D**, **G**, **J**, **M**, and **P**) The materials and operation steps. (**B**, **E**, **H**, **K**, **N**, and **Q**) The reaction time for optimal colorimetric readouts. (**C**, **F**, **I**, **L**, **O**, and **R**) The linearity for color intensity versus concentrations; for ALB, TP, Cl^-, ALP, ALT, and AST, respectively. The inserted figures in (C), (F), (I), (L), (O), and (R) are UV-vis spectroscopy results and the inserted pictures are the colorimetric images under different biomarker concentrations.

The assays for AST and ALT involve similar processes where different substrates specific to each enzyme—alanine for ALT and aspartic acid for AST—are decomposed into pyruvic acid. This pyruvic acid then reacts with dinitrophenylhydrazine (DNPH), forming 2,4-dinitrophenylhydrazone (2,4-DNPH), which produces a brown color upon the addition of an alkaline substance (Fig. 2, M and P). We assessed the absorbance of ALT and AST at 1, 2, 3, and 4 min (Fig. 2, N and Q). At 3 min, both assays demonstrated strong linearity, with an R^2 value of 0.98 at 505 nm (Fig. 2, O and R) and a coefficient of variation of less than 3% (10 U/liter). Although the absorbance increased slightly at 4 min (approximately 5%), the performance declined, with linearity decreasing to $R^2 = 0.95$ and CV increasing to around 6%. Considering both detection efficiency and measurement accuracy, we selected 3 min as the optimal reaction time for the ALT and AST assays. In addition, the AST/ALT ratio is a valuable diagnostic tool in liver disease assessments. For instance, a ratio of greater than 2 is commonly associated with alcoholic liver disease, while a ratio of less than 1 is indicative of NASH and viral hepatitis—though it may rise above 1 as cirrhosis progresses (*39*, *40*).

Energy-embodied microfluidics

Charging and storage of pressurized gas

The EE-POCT device consists of a cover layer, a plastic film, an elastic film, adhesives, and a channel layer (Fig. 1D). The elastic film, made of thermoplastic polyurethane (TPU) with low gas permeability, is bonded to the channel layer using AR 90880 adhesives. Mechanical clamping structures on the cover layer enhance the sealing performance. The size parameters of the platform are 80 mm by 73 mm by 8 mm (length × width × thickness). Detailed information for the size parameters can be found in fig. S1. Detailed fabrication and device specifics are provided in Materials and Methods and fig. S2. To charge the device with pressurized gas, the switch on the cover layer is activated, allowing the gas to flow into the chamber. Deactivating the switch triggers the end side of the switch to compress a flexible protrusion of the elastic film into the channel, effectively sealing it to prevent gas leakage (Fig. 3A and movie S1). A plastic film is placed atop the elastic film to ensure the smooth transition of the switch during activating and deactivating operations. Several tests were conducted to assess the stability of the energy-embodied

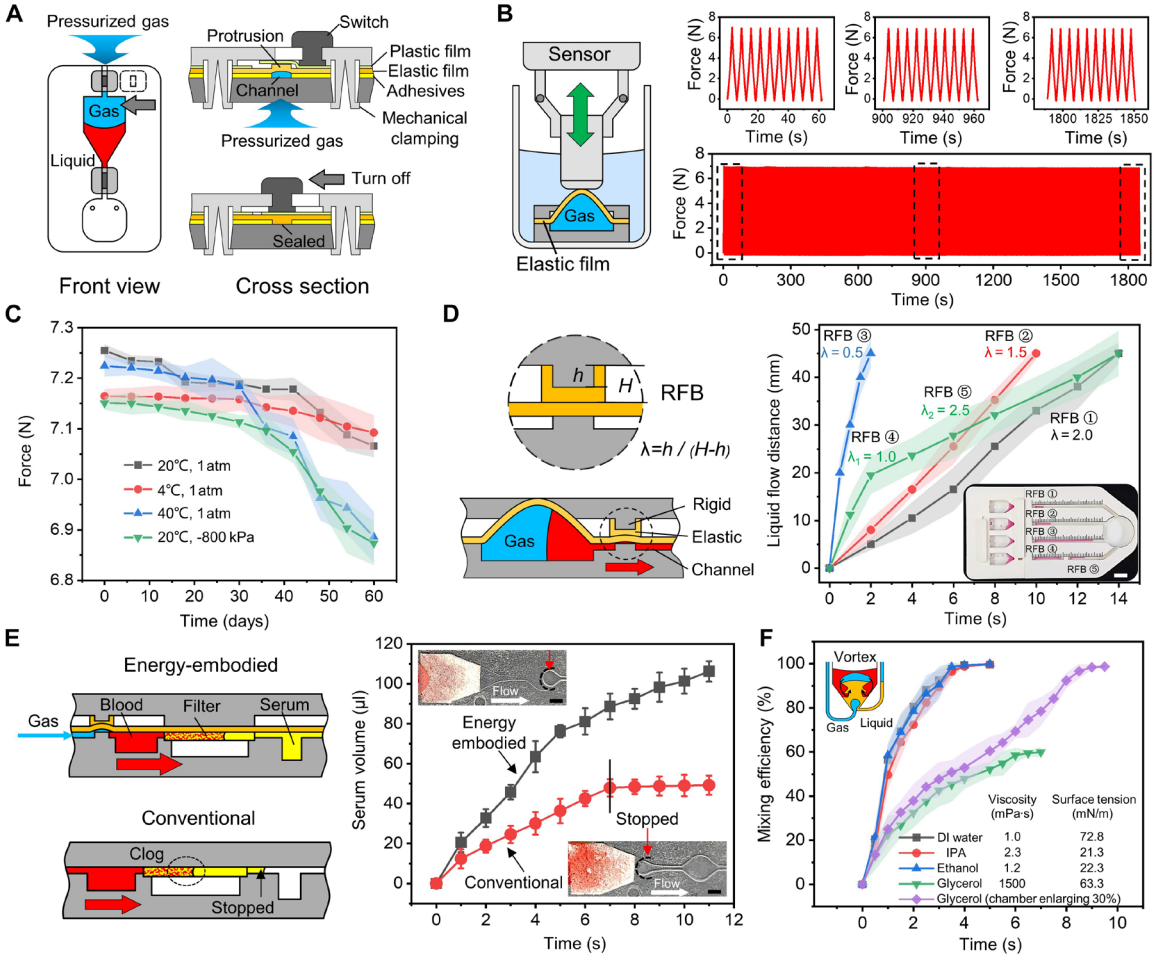

Fig. 3. Design and working principles of the energy-embodied microfluidics. (**A**) Schematic of the device components and the charging process of pressurized gas. By one-step turning off the switch, pressurized gas can be robustly stored in the chamber. (**B**) Sealing performance of the EE device by pressing the elastic film using a tensile machine for 300 cycles. (**C**) Storage characterization under various temperatures and pressures. (**D**) Mechanism and results for the programmable flow tests. The inset is the device used in the testing process. (**E**) Comparison of the energy-embodied and conventional whole blood filtering. The inset is the picture of the flow behavior with the dashed lines indicating the flow surface. (**F**) Vortex mixing results. For all the above experiments, three independent experiments were conducted with the data shown as ±SD. Scale bars, 6 mm.

(EE) chamber. After sealing the channel (switch off), the EE chamber endured a 300-cycle pressing test (compression ratio of 50%) using a universal tensile machine (Instron 5943, USA), showing no notable decrease in gas pressure (Fig. 3B and movie S2). The chamber's burst pressure was measured at 258.7 kPa (movie S3). Regarding long-time gas storage, tests showed minimal change in gas pressure (a decrease of only 1.3%) after 60 days at 20°C and 1 atm, or at 4°C and 1 atm. At higher temperatures or under negative atmospheric pressure (40°C, 1 atm or 20°C, −800 kPa), the pressure decreased by about 4.2%, likely due to increased gas permeation rate (Fig. 3C). The microfluidic flow performance after 60 days of storage showed no notable difference compared to that of a newly made device, suggesting that the system is not overly sensitive to minor variation in gas pressure.

Programmable flowing

The device incorporates a rigid-flexible block (RFB) structure to adjust the flow rate, consisting of a cylindrical rigid part on the cover and a flexible part made of Ecoflex 30 with a Young's modulus of 100 kPa. We define a parameter, $\lambda = h/(H - h)$, representing the ratio of the height of the rigid part (h) to the flexible part (H), to establish a relationship between the RFB size and the flow rate (Fig. 3D). The flow rate can be precisely controlled within a range of 1.1 to 11.0 μl/s by varying λ values between 0.5 and 2.5. Specifically, altering λ to 2.5 at the midpoint of the microchannel allows the flow rate to vary from 4.9 down to 1.1 μl/s. The programmable flow performance can be seen in movie S4.

Clog-free filtering

Traditional POCT devices often use paper-based blood filters, which can become clogged due to spontaneous capillary flow in the micrometer-diameter fiber filaments of the paper, leading to ineffective filtering performance (*41*). To address this, we use pressurized gas to achieve clog-free filtering, where controlling the gas releasing rate is critical for successful filtration. If the gas releases too rapidly, blood cells can bypass the filter and enter the chamber. By using an RFB with a λ value of 1.5 to moderate the gas release rate, we were able to separate approximately 100 μl of serum from whole blood samples in just 10 s. In contrast, using conventional spontaneous filtering methods, only 40 μl of serum could be obtained (Fig. 3E and movie S5).

Vortex mixing

While various mixing techniques such as serpentine mixing (*42*), chaotic mixing (*43*), and batch-mode mixing (*44*) have been explored for liquid mixing on POCT platforms, their efficiency and effectiveness often remain unsatisfactory. We have implemented a vortex mixing method that uses pressurized gas to enhance mixing performance. In this method, pressurized gas is introduced into the bottom of the mixing chamber through a separate gas chamber, generating air bubbles that create a strong vortex that enables complete mixing of the liquid contents within just a few seconds. Figure 3F shows the mixing results for liquid with varying viscosities and surface tensions. It can be seen that the surface tension has minimal impact on mixing efficiency. For instance, deionized water with a surface tension of 72.8 mN/m and isopropyl alcohol with a surface tension of 21.3 mN/m both achieved complete mixing within approximately 3 s. This suggests that the mixing process is primarily driven by the prestored pressured air, reducing the need for surface hydrophilic/hydrophobic treatment when handling polar liquids. In contrast, increased viscosity notably affects mixing performance. When the viscosity was increased to 1500 mPa·s (glycerol), the mixing efficiency dropped to approximately 60% after 6 s of vortex mixing. However, full mixing could still be achieved by allowing the chamber to expand by 30%, extending the mixing time to about 9 s. All experiments were conducted using a constant prestored air pressure of 60 kPa. The vortex mixing video and the captured mixing images can be found in movie S6 and fig. S3. Detailed calculations of mixing efficiency are outlined in Materials and Methods.

Time-selective releasing

Time-selective releasing is crucial for multiplexed POCT that involves multiple reaction steps and different curing times within a cost-effective and autonomous device. Our EE microfluidics design tackles prevalent challenges, such as low sensitivity and high dead volume by incorporating a mechanical pressure sensing timer (MPST). Figure 4A demonstrates a flowchart to elaborate the mechanism of MPST. Upon energy charging, the pressurized gas expands the elastic film, pushing the lever upward, thereby sealing the liquid channel. When the switch is activated, gas is released through the channel at a rate controlled by the RFB. As the λ values of the RFB increase, the rigid portion becomes dominant, more effectively sealing the air channel and thus slowing gas release. Conversely, a lower λ value results in a softer RFB, allowing the pressurized gas to escape more readily. For example, the gas release rate is approximately 6.2 μl/s at $\lambda = 0.8$, which drops to about 0.83 μl/s when λ increased to 2.0 (Fig. 4B). More detailed information about the gas releasing process can be found in fig. S4 and movie S7. As the gas pressure P decreases below the critical pressure P_c, the lever tip disengages from the elastic film, opening the liquid channel and initiating reagent release. We developed an analytical model using beam theory to calculate this critical pressure P_c, which is detailed in the Supplementary Text and fig. S5. The liquid channel opens when $P_c \leq \frac{2T_x^*}{SL}$, where T_x^* is the torque generated by the bending deformation of the hinge, S is the contact area of the lever with the elastic film, and L is the lever length. The experimental data align well with our analytical model (Fig. 4C), confirming that the critical pressure P_c decreases as L increases, consistent with the classical beam model. By correlating the internal gas pressure over time to the critical pressure model, we derived linear fitting curves between liquid holding time and parameter λ (Fig. 4D). These curves enable prediction of liquid holding time, essential for optimizing the design of the EE-POCT device. The flow behavior video is provided in movie S8.

EE-POCT device and colorimetric algorithm

Figure 5A illustrates a schematic of a typical EE-POCT device, featuring multiple chambers (from #0 to #N), MPSTs, resistors, one reaction chamber, and switches. Figure 5B shows the EE-POCT device configured for different essay types: a one-step assay (ALB, TP, and Cl^-), a two-step assay (ALP), and a three-step assay (AST and ALT). The preparation and application processes for the EE-POCT device are provided in Fig. 5 (C and D). Initially, various reagents are loaded into chambers #2 through #N according to the required number of reaction steps. Subsequently, pressurized gas is introduced into chamber from #1 to #N and switch S1 is deactivated to seal it. This prepares the EE-POCT device for storage or distribution to users. The stability of the prestored reagents, crucial for liver function monitoring, was evaluated under various environmental conditions, as shown in fig. S6. The assay performance remained consistent after 30 days of storage at −4° and 4°C, with humidity maintained at 40% relative humidity (RH). However, at elevated temperatures of 25° and 40°C, a noticeable decline in performance

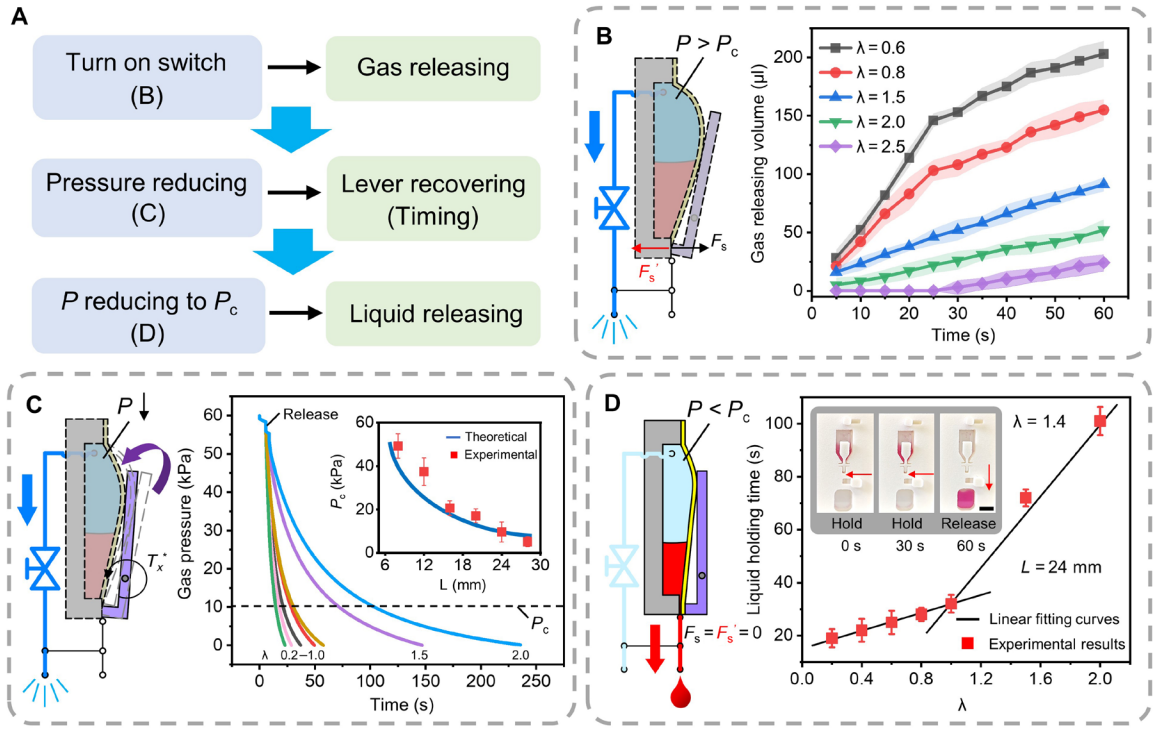

Fig. 4. Mechanism of time-selective releasing. (**A**) Flowchart illustrating the relationship between the pressure release process of MPST and time control. (**B**) Upon activating the switch, the prestored gas is released, and the release rate is regulated by the parameter λ of RFB. (**C**) As the pressure decreases, the MPS lever gradually returns to its original position, determining the timing behavior. The plot shows the relationship between release time and gas pressure in the chamber. The inset compares the critical pressure versus MPS lever length based on both theoretical modeling and experimental data. (**D**) When the pressure *P* reducing to critical pressure P_c, the liquid in chamber is released. A linear curve of the parameter λ and the releasing time is presented. The inset shows representative experimental images for λ = 1.4. For all the above experiments, three independent experiments were conducted with the data shown as ± SD. Scale bars, 6 mm.

was observed after 5 days, particularly for the ALT and AST reagents. At 4°C, variations in humidity (20, 40, and 80% RH) did not affect assay performance, likely due to the platform's airtight design, which helps protect the reagents from moisture exposure. For real-world deployment, the platform should be stored and transported at 4°C. If exposed to higher temperatures, it is recommended that the device be used as soon as possible to ensure optimal performance. Upon receipt by users, samples are injected into chamber #0 and switch S2 is deactivated to seal the sample chamber. Activation of switch S3 then allows the pressurized gas from chamber #1 to drive the sample into the reaction chamber. Subsequently, reagents from chambers #2 to #*N* are released and mixed in the reaction chamber in a time-selective manner, controlled by the preprogrammed parameter λ in the MPST. It is important to note that resistors, configured as narrowed or serpentine microchannel within the device, prevent the reagents from flowing into unintended channels or chambers.

Figure 5E outlines the colorimetric analysis strategy to mitigate the effects of ambient light intensity and color variations. As detailed in Materials and Methods and fig. S7, a color checker with a known color space is applied into the EE-POCT device. The color accuracy of the standard color checker is maintained through standard color calibration and the user of a high-fidelity printer (*45*). Environmental conditions can alter the color space values of the color checker. By comparing the changes in color space between the captured and the standard color checker, a correction factor is derived. This factor is then applied to the colorimetric readings to produce corrected and standardized results. This method does not require the tedious training process for the machine learning prediction method (*16*, *17*), and it also can be readily applied to different smartphone platforms. The efficacy of this approach is demonstrated in fig. S8, where it is evident that the RGB values of the captured image show substantial variations under different environmental color temperatures (SD = 48.1 for the blue channel of well 1). However, with the implementation of the colorimetric analysis algorithm, this variation is substantially reduced (SD decreased to 4.3 under the same conditions). In addition, the algorithm's cross-platform capability was tested using smartphones with IOS and Android operation systems. The results confirmed that, without any configuration steps, the RGB values and their variations remain consistent across different smartphone platforms under varying color temperature conditions.

In the one-step assay (ALB, TP, and Cl^-), upon activation of switch S3, the sample is rapidly propelled into the reaction chamber by the pressurized gas from chamber #1, taking approximately 4 s for the colorimetric reagents to flow and mix within the reaction chamber (λ = 0.1, *L* = 10 mm). For the two-step assay (ALP), following the initial reagent introduction and mixing under the same condition as the one-step assay (λ = 0.1, *L* = 10 mm), a subsequent injection and mixing of the second reagent occur, also taking an additional 4 s (λ = 0.3, *L* = 10 mm). In the three-step assay (AST and ALT), the process accommodates necessary substrate decomposition time, set at 3 min before the addition and mixing of the terminating reagents (λ = 3.0, *L* = 10 mm). A further 4 s is then required for the

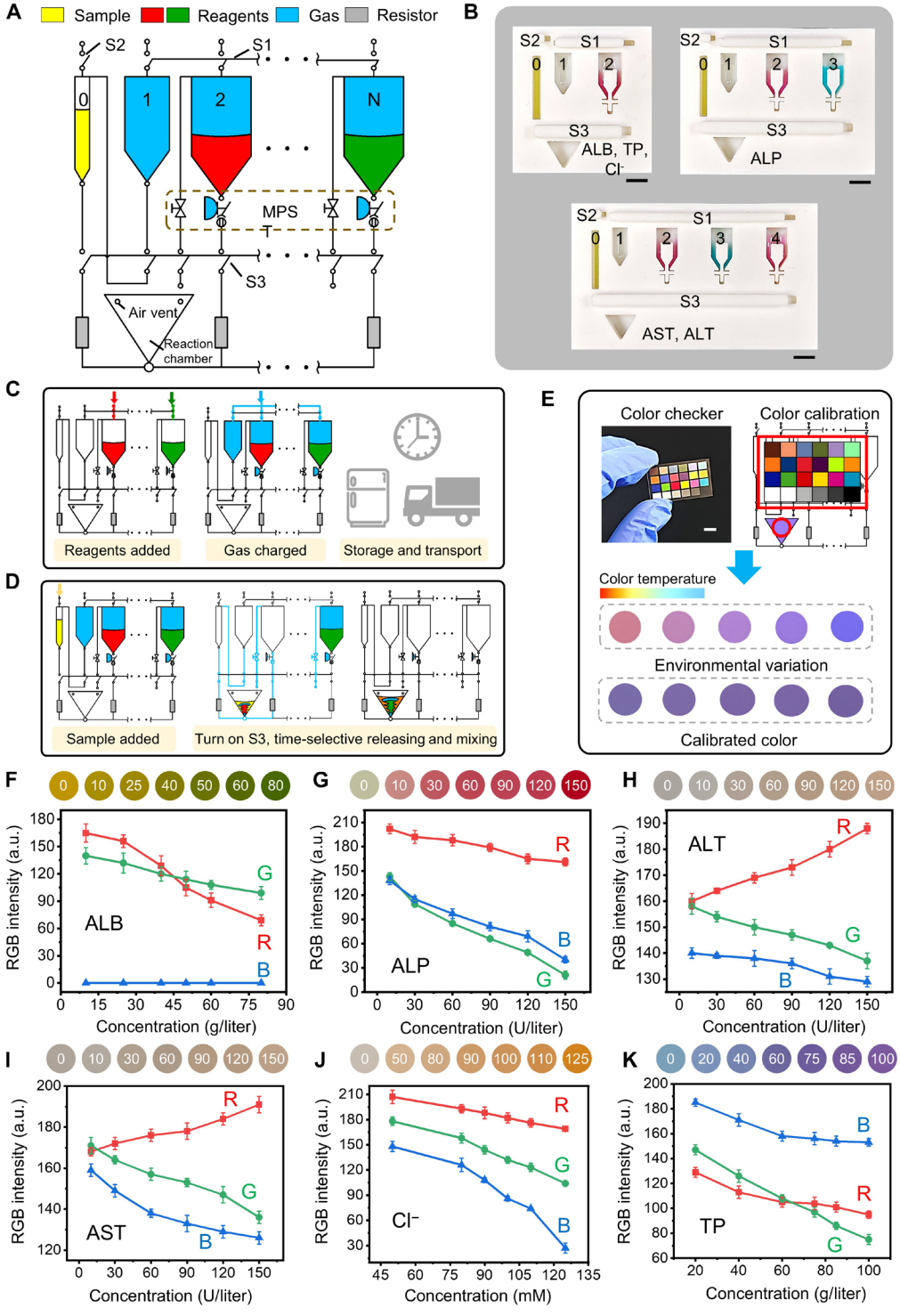

Fig. 5. EE-POCT device and colorimetric analysis for multiplexed biomarkers. (**A**) Schematic view of the EE-POCT device with mechanical pressure self-sensing timer (MPST), resistor, and switches. (**B**) The pictures of three EE systems for biomarkers with different operation steps. (**C**) The preparation and (**D**) application of the EE-POCT device. (**E**) Color analysis method using a standard color checker. Standard calibration curves between RGB value and concentration of markers for (**F**) ALB, (**G**) ALP, (**H**) ALT, (**I**) AST, (**J**) Cl^-, and (**K**) TP. For all the above experiments, $n = 3$ independent experiments were conducted with the data shown as ±SD. Scale bars, 6 mm.

third reagent's introduction and mixing ($\lambda = 3.2$, $L = 10$ mm). The flow behavior of the EE-POCT device is provided in movie S9. A linearity test by using the EE-POCT device and the colorimetric algorithm was conducted by spiking known amounts of purified markers to artificial blood serum buffer. The limits of detection (LOD) were established for ALB, ALP, ALT, AST, Cl^-, and TP as 6.8 g/liter, 5.3 U/liter, 7.9 U/liter, 8.8 U/liter, 18.3 mM, and 11.6 g/liter, respectively, in the G channel of RGB images (Fig. 5, F to K). The coefficients of variation for the biomarkers ALB, ALP, ALT, AST, Cl-, and TP are 6.4, 3.5, 1.9, 2.3, 2.8, and 2.7%, respectively, at low concentrations of 10 g/liter, 10 U/liter, 10 U/liter, 10 U/liter, 50 mM, and 20 g/liter, based on three independent experiments. The detailed information about the linearity test is provided in Materials and Methods and fig. S9. By using the calibration curves and the colorimetric algorithm, the colorimetric readouts under various color temperatures (2700 to 6500 K) remained consistent with the true values. Without the algorithm, notable color variations were observed, compromising the data's credibility (fig. S10).

Clinical validation using an all-in-one EE-POCT platform

We have developed an all-in-one EE-POCT platform capable of managing 11 different reagents simultaneously to achieve quantitative colorimetric readouts for six direct liver-related biomarkers (ALB, TP, Cl^-, ALP, AST, and ALT) and three indirect ones (GLB, ALB/GLB ratio, and AST/ALT ratio). This integrated system includes six reaction chambers, one whole blood filtering chamber, and 12 separate rigid-flexible chambers, where 11 of them are used for storing reagent and 1 is used for pumping the sample into the reaction chamber (fig. S11). As illustrated in Fig. 6A, users simply introduce a 180-μl whole blood sample in the sample inlet and activate the switch, and the platform automatically executes the test procedure based on preprogrammed λ values of the RFB. The testing sequence is efficiently timed: approximately 10 s for whole blood filtering and serum aliquoting, 4 s for releasing and mixing the first set of parallel reagents, another 4 s for the second round (second-step reactions for ALP), 3 min for the third round (curing time for the second-step reactions for AST and ALT), and, lastly, 4 s for the fourth round (third-step reactions for AST and ALT). This results in a total turnaround time of under 4 min. The schematic view and the flow manipulation details are provided in movie S10 and Fig. 6B. Upon completion of the testing process, a smartphone captures the colorimetric image (Fig. 6C), whereupon a custom mobile application analyzes and corrects color accuracy to output quantitative testing results (details in Materials and Methods and movie S11). Our proposed EE-POCT showed a certain advantage over the current POCT technologies, in terms of accuracy, efficiency, affordability, equipment-free, and multiplexing capabilities (Fig. 6D).

To assess the clinical applicability of our all-in-one EE-POCT, we conducted a study involving whole blood samples from 103 volunteers. The study was approved by The First Affiliated Hospital of Zhejiang University (IIT20240106B-R1) and Westlake University (20240415JHQ001). Each sample was divided into two aliquots: one tested using our EE-POCT device and the other using a commercial blood analyzer (Beckman Coulter, AU5800), serving as the gold standard. Direction comparison results, provided in Fig. 7 (A to F), demonstrate good concordance between the EE-POCT and the commercial blood analyzer, with Pearson coefficients exceeding 0.9. The Bland-Altman analysis (Fig. 7, G to L) further confirmed the reliability of our device, indicating that above 97% of the results were within the 95% limits of agreement. The specific limits of agreement for ALB, TP, Cl^-, ALP, AST, and ALT were −4.6 to 8.7 g/liter, −7.8 to 9.6 g/liter, −3.2 to 4.6 mM, −13.7 to 19.5 U/liter, −6.5 to 13.7 U/liter, and −5.5 to 14.4 U/liter, respectively. An outlier was observed in the ALP measurements, where the blood analyzer reported 356.9 U/liter and the all-in-one EE-POCT measured 277.3 U/liter, both notably above the NCR of 50 to 135 U/liter for ALP. This discrepancy likely occurred because the ALP level exceeded our device's test capability. It is important to note that there are no marker levels that blood analyzer values >1× upper limit of normal (ULN) that were read by the all-in-one EE-POCT within ULN. Similarly, there were also no marker levels that blood analyzer values within ULN that were read by the all-in-one EE-POCT >1× ULN. Because the 1× to 3× ULN is critical to determine the level of the liver injury (*40*), these results suggest clinically acceptable agreement between the all-in-one EE-POCT and the gold standard assay method. The results for the indirect indicators (GLB, AST/ALT ratio, and ALB/GLB ratio), which can be derived from the direct marker, are provided in fig. S12.

Assessments of the correlation between liver biomarkers and specific liver diseases

To study the correlation between liver biomarkers and specific liver diseases, 12 blood samples from healthy individuals and 36 blood samples from diagnosed patients with conditions of fatty liver ($n = 15$), viral hepatitis ($n = 8$), cirrhosis ($n = 7$), and liver cancer ($n = 6$) were tested using the EE-POCT platform (Fig. 8A), with the commercial blood analyzer AU5800 for comparison. Figure 8 (B and C) shows that transaminases levels (AST and ALT) in fatty liver samples were all below 1× ULN, with some even within the NCR. This is likely due to limited liver cell damage at this stage, allowing the liver to maintain normal function through its compensation mechanism. In viral hepatitis samples, transaminase levels ranged from 1× to 3× ULN. For cirrhosis and liver cancer, however, transaminase concentrations decreased to below 1× ULN, with one liver cancer sample showing an ALT level (3.7 U/liter) even below the lower limit of normal range (7 U/liter). This decrease may be attributed to extensive cell death or severe damage in cirrhosis and liver cancer, which impairs the liver's ability to synthesize transaminase, resulting in their decreased concentration in serum. Figure 8D shows that the AST/ALT ratio decreases to below 0.5 in some cases of viral hepatitis, while it increases to around 2 in liver cancer, likely due to reduced clearance of AST secondary to impaired function of sinusoidal cells (*38*, *40*).

Figure 8E shows that ALP levels for fatty liver were within the NCR, but were elevated in viral hepatitis, cirrhosis, and liver cancer, which aligns with previous findings that liver damage in these diseases impairs to excrete ALP produced by the bone, intestine, and liver (*46*). Serum protein concentrations in fatty liver and viral hepatitis cases were within the NCR, while in patients with cirrhosis and liver cancer (Fig. 8, F and G), protein levels were notably reduced, likely due to decreased ALB synthesis associated with chronic liver disease like cirrhosis. For GLB concentration, the biomarkers remain within or near the NCR (Fig. 8H). However, the ALB/GLB ratio decreases to below 1 in some liver cancer cases, which may be due to the dysfunction of ALB synthesis, leading to a severe reduction in ALB concentration in these patients (Fig. 8I). In some liver cancer cases, chloride levels were also below the NCR (Fig. 8J), indicating substantial liver dysfunction and impaired nutrition

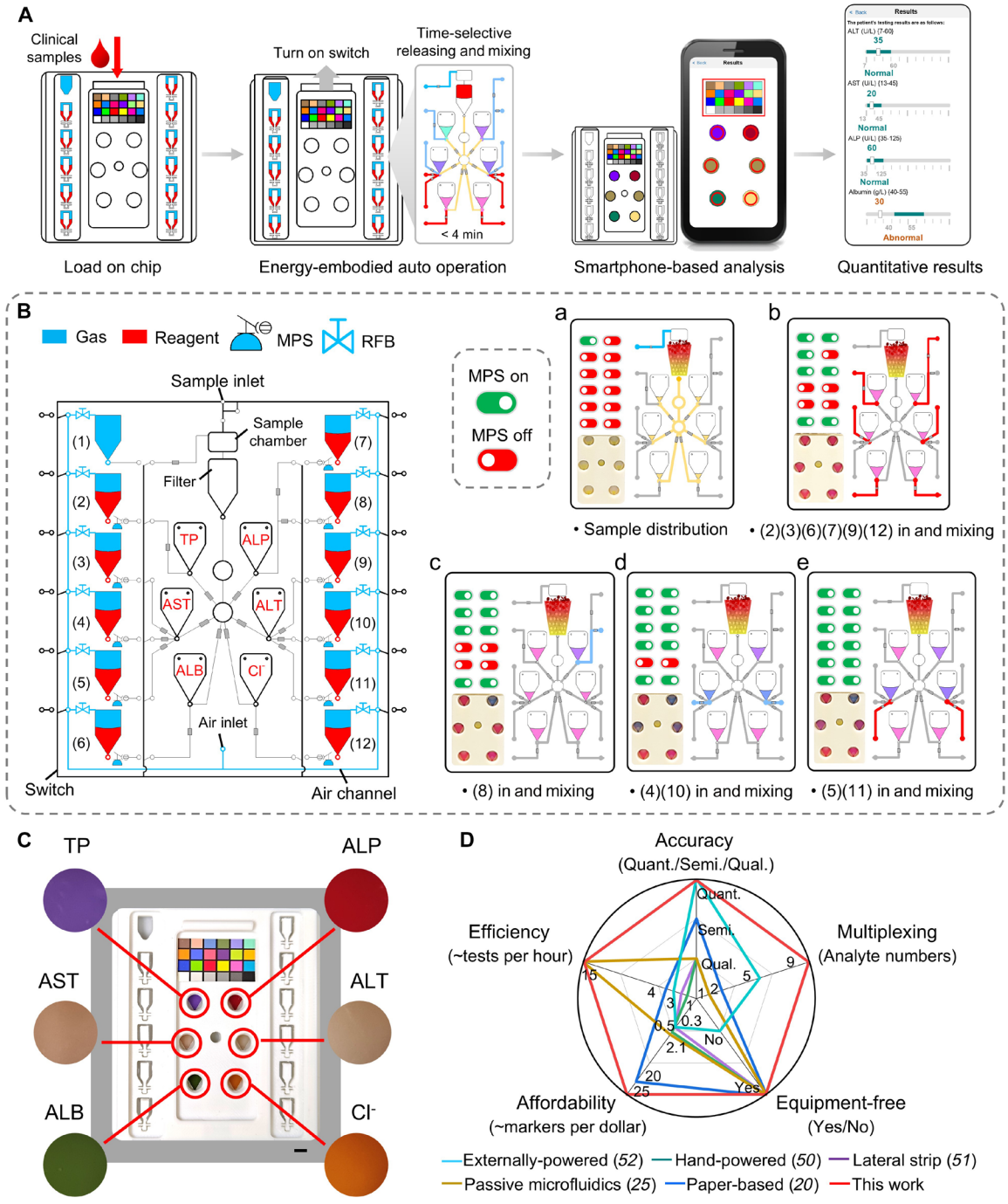

Fig. 6. Demonstration of an all-in-one EE POCT system. (**A**) Working flow of the all-in-one EE system. The users only need to add 180 μl of whole blood sample and turn on the switch; within 4 min, the system is capable of dealing with the prestored 11 reagents and achieving nine direct and three indirect quantitative results. (**B**) Schematic view of the all-in-one EE POCT system with (a) to (e) demonstrating the energy-embodied auto operation procedures. (**C**) Picture of the system and the colorimetric readouts for the six detection zones. Scale bar, 6 mm. (**D**) Radar image for the comparison on the current POCT technologies (*20*, *25*, *50*–*52*).

metabolism, leading to water-electrolyte imbalances and reduced sodium, potassium, and chloride levels (*46*).

Distinct patterns of different liver biomarkers for each condition were thus found in this study. Liver function markers for fatty liver were generally within the NCR, except for a slight increase in ALT and AST levels, typically below 1× ULN. For viral hepatitis, ALT and AST levels were notably elevated, often reaching 1× to 3× ULN. For cirrhosis and liver cancer, ALT and AST levels followed a trend similar to that in fatty liver (around 1× ULN), though protein levels were markedly reduced. In certain liver cancer cases, chloride levels fell below the NCR, which could serve as an indicator of disease severity. Although transaminases (ALT and AST) are commonly used

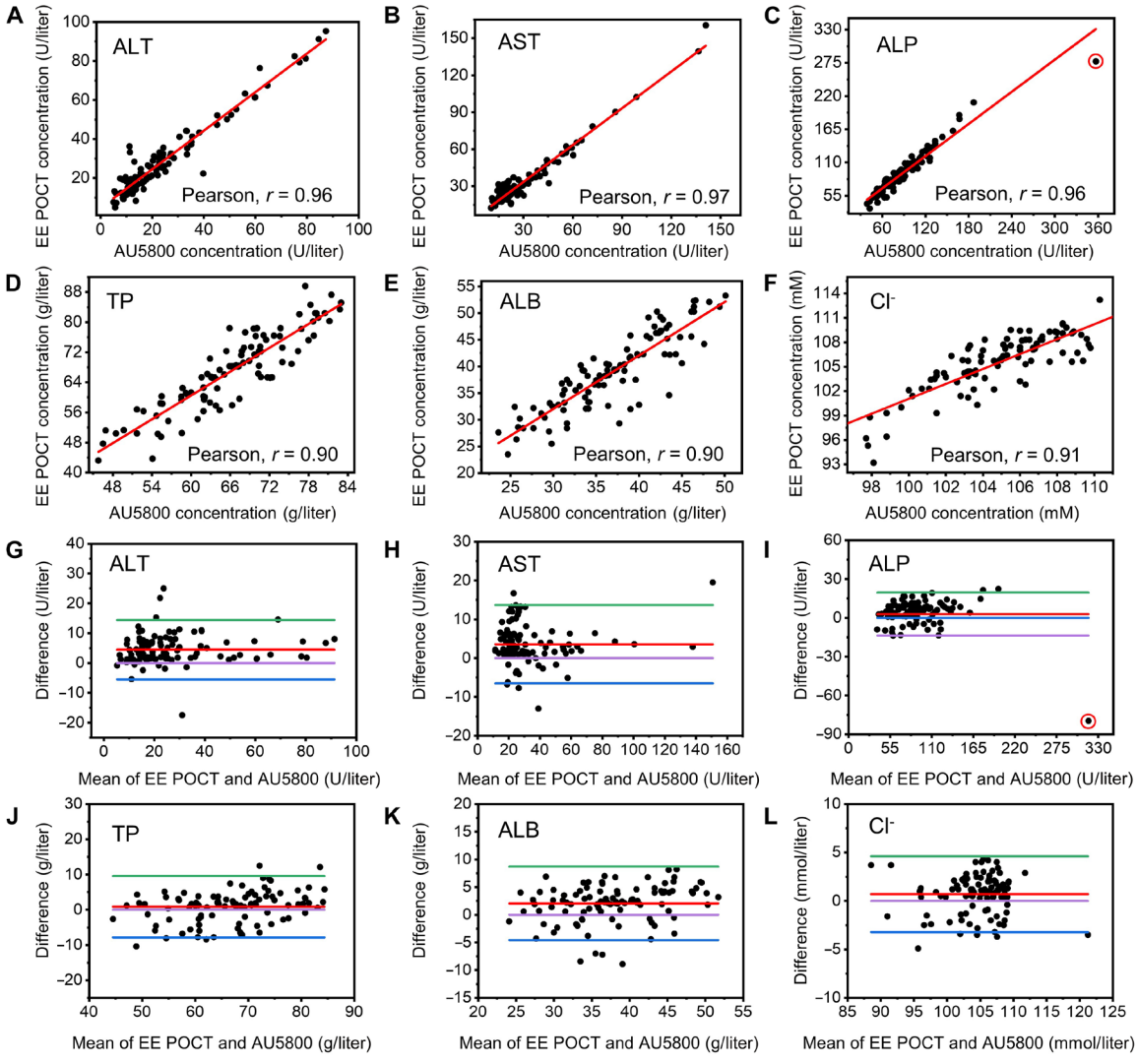

Fig. 7. Clinical validations using the all-in-one EE POCT system. Direct comparison of the quantitative results made by the system and the standard commercialized analyzer (AU5800) for (**A**) ALT, (**B**) AST, (**C**) ALP, (**D**) TP, (**E**) ALB, and (**F**) Cl^-. The red line corresponds to the line of equality. The red circle in (C) is deviated data. (**G**), (**H**), (**I**), (**J**), (**K**), and (**L**) are Bland-Altman plots of the testing in clinical samples for ALT, AST, ALP, TP, ALB, and Cl^-, respectively. The green and blue lines represent the 95% limits of agreement. The purple line is the line of equality, and the red line is the average different of the methods. The red circle in (I) is obvious deviated data.

as specific indicators of liver injury, they may not always provide reliable diagnostic results for fatty liver and cirrhosis. It should be noted that fatty liver is reversible under proper treatment, whereas cirrhosis is irreversible (*40*), highlighting the importance of comprehensive liver function monitoring (including ALP, proteins, chloride, and other markers) to prevent the progression from mild fatty liver to severe cirrhosis or liver cancer. These findings underscore the value of using a comprehensive panel of biomarkers to distinguish between liver conditions and to monitor disease progression, potentially guiding more effective management and prevention strategies.

DISCUSSION

The rising incidence of liver injuries underscores the critical need for a comprehensive liver function monitoring; however, a limited set of biomarkers often fail to provide an accurate discrimination of liver damage from mild NAFLD to severe cirrhosis. To achieve multiplexed testing with clinical accuracy, paralleled reagent manipulation where different reagents react in separate chambers for different biomarkers is often required to avoid unintended nonspecific adsorption and reagent interference. Traditionally, the paralleled reagent manipulation has relied on centralized laboratories equipped with costly devices and operated by trained professionals, limiting accessibility in resource-poor areas. To address these challenges, we developed a cost-effective, quantitative, and multiplex POCT platform that overcomes many limitations of existing POCT technologies such as high costs of externally powered systems, the inadequate accuracy of passive microfluidics, and the need for excessive user intervention in hand-powered devices.

This study introduces an EE-POCT technology, which integrated the driving and manipulation energy with the liquid reagents and

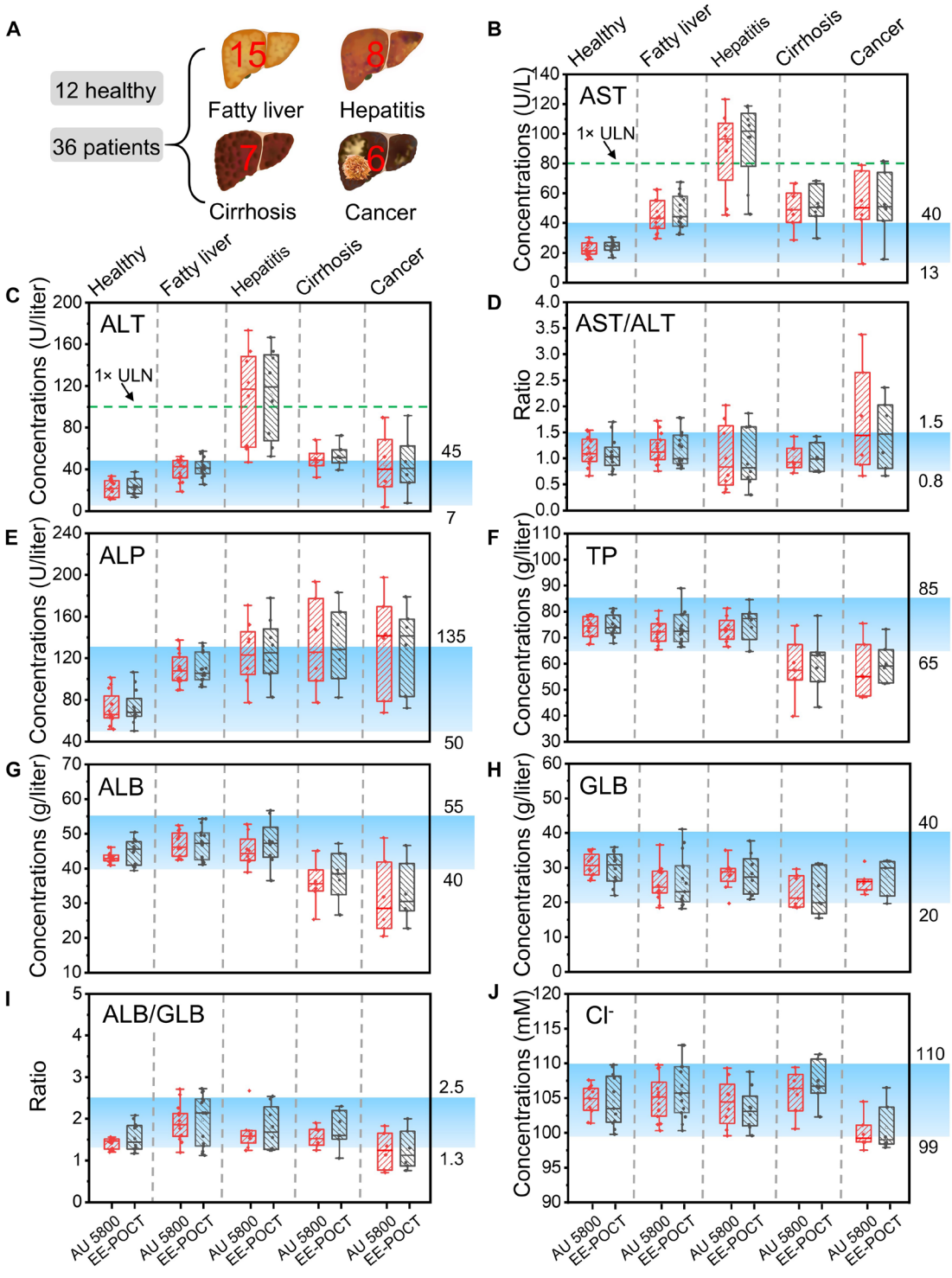

Fig. 8. Correlations between biomarkers and specific liver diseases. (**A**) Samples of healthy individuals (n = 12), fatty liver (n = 15), viral hepatitis (n = 8), cirrhosis (n = 7), and liver cancer (n = 6) used in the experiments. Box-and-whisker plot of the concentrations of (**B**) AST, (**C**) ALT, (**D**) AST/ALT, (**E**) ALP, (**F**) TP, (**G**) ALB, (**H**) GLB, (**I**) ALB/GLB, and (**J**) Cl^-. For each plot, the central black mark indicates the median, and the bottom and top lines of the box indicate the 25th and 75th percentiles, respectively. The whiskers extend to the min-max data points that were not considered outliers. The blue bands in the plots indicate NCR for each biomarker. The green dashed lines in (B) and (C) mean the ULN.

demonstrating several features: (i) an EE microfluidic system that facilitates paralleled reagents manipulation including independently time-selective releasing, vortex mixing, programmable flowing, clog-free blood filtering, and reagent storage without the need for electricity or any equipment; (ii) low-cost colorimetric assays for six critical liver injury biomarkers; (iii) a robust colorimetric analysis algorithm that enhances color accuracy and ensures cross-platform performance capabilities [validation with 103 clinical samples demonstrated that our platform could deliver simultaneous and quantitative results for nine liver-related indicators (ALB, ALP, Cl^-, AST, ALT, TP, GLB, AST/ALT ratio, and ALB/GLB ratio) within 4 min, showing excellent concordance with a clinical gold standard analyzer (Pearson coefficients >0.9 for all the indicators) and achieving cost-effectiveness at $0.40 per test (table S2)]; and (iv) assessments of the correlation between the liver biomarkers and the liver diseases (fatty liver, hepatitis, cirrhosis, and liver cancer), which may provide a reference to the diagnosis of the liver diseases.

Unlike electrochemical and optical test methods, which require sophisticated equipment, trained personnel, and considerable processing time, colorimetric assays are simple, inexpensive, and require minimal equipment, making them especially suitable for decentralized use. Our EE-POCT technology not only improves the traditional colorimetric approach by enhancing reaction kinetics and mixing efficiency but also addresses the influence of external factors like ambient light and reagent instability. This adaptability ensures that the platform can deliver reliable diagnostics under a variety of conditions.

Looking forward, leveraging advances in chemical and biological engineering could expand the range of detectable diseases using colorimetric methods. Research into colorimetric reagents and the integration of nanotechnology and synthetic biology may enable the detection of a broader array of biomarkers, including those associated with infectious diseases and cancers (*47*–*49*), which are traditionally identified using more complex systems. This work not only signifies a substantial improvement over existing POCT technologies in terms of accessibility, efficiency, and cost but also highlights the potential of colorimetric assays—when integrated into innovative platforms like EE-POCT—to expand medical diagnostics. Such advancements align closely with global health objectives to enhance diagnostic capabilities universally, ensuring that rapid, reliable, and affordable diagnostics are accessible to all, thus improving health outcomes worldwide.

As we advance, we aim to potentially expand the scope of EE-POCT to include diagnostics for other conditions such as heart and kidney diseases. In addition, we plan to enhance the long-term storage stability of our device, particularly at room temperature, to better meet the needs of various clinical settings.

MATERIALS AND METHODS

Study participants

The collection and use of human whole blood samples (103 specimens) were approved by the ethics committee of the First Affiliated Hospital of Zhejiang University (IIT20240106B-R1) and Westlake University (20240415JHQ001). Informed consent was obtained from all the participants. The participants volunteered to be tested with no compensation.

Materials and reagents

The purified markers ALT, AST, ALP, ALB, TP, and Cl^-, and reagents Bromo-cresol green, copper sulfate, sodium hydroxide, mercuric thiocyanate, DPP, 4-aminoantipyrine, PF, alanine, aspartic acid, and DNPH were all purchased from Aladdin, China. The polyethylene terephthalate (PET) film and the TPU film were purchased from Xinrui, China. The adhesives were purchased from Adhesive Research, USA. Ecoflex 30 was purchased from Smooth-on, USA. The 3D-printing material polylactic acid (PLA) was purchased from Raise3D, China.

Fabrication of the EE-POCT device

The channel layer and cover of the EE-POCT device were made of PLA materials and were 3D printed using an Ender 3 Pro 3D printer (Shenzhen Creality 3D Technology Co. Ltd.). After 3D printing, the surface of the channel layer was polished using 800-grit sandpapers (3M, 407Q), decreasing the surface roughness from about 24 μm to below 0.1 μm. The double-sided adhesives and 100-μm-thick PET film were both cut using a Silhouette Cameo 2 cutter from Silhouette America Inc. The TPU film was bonded to the channel layer using the adhesives by hot pressing in the temperature of 45°C for 10 min. Then, the PET film was covered onto the TPU film, and the cover was applied to the channel layer through the mechanical clamper. The elastic blocks were made of Ecoflex 30 by casting the mixture of part A:part B = 1:1 to a 3D-printed mold and cured for 20 min at a temperature of 50°C. The pictures of the components and fabricated process are provided in fig. S1.

Characterization of the EE microfluidics

The sealing performance was conducted by placing the rigid-elastic chamber in the water and pressing the chamber through a universal tensile machine (Instron 5943) at a speed of 1 mm/s for 300 cycles. The pictures of the programmable flowing, clog-free filtering, gas releasing, vertex mixing, and time-selective releasing were all taken using a high-speed camera (Sony AX700 with 1000 frames/s). An air compressor was used to generate the air pressure, and a digital precision pressure regulator was used to adjust the value of the pressure. The flow behavior testing process is as follows. A given amount of liquid was injected into the testing device and a high-speed camera was applied to record the flow behavior. The still images were then captured from the flow behavior video at fixed time points and the remaining area was calculated using the software Image-Pro Plus and then multiplied by the depth of the chamber to calculate the volume. The mixing efficient can be achieved using the following equation (*42*)

$$M = 1 - \sqrt{\frac{1}{N}\sum_{i=1}^{N}\left(\frac{c_i - \bar{c}}{\bar{c}}\right)}$$

where M is the mixing efficiency, N is the total number of sample pixel points, and c_i and $\bar{c}$ are normalized concentration and expected normalized concentration, respectively. Mixing efficiency ranges from 0 (0%, not mixing) to 1 (100%, full mixed).

Colorimetric analysis algorithm

The color space of the captured image of the color checker can be expressed as

$$S_l = \begin{bmatrix} R_{l1} & G_{l1} & B_{l1} \\ R_{l2} & G_{l2} & B_{l2} \\ \cdots & \cdots & \cdots \end{bmatrix}$$

The color space (known) of the standard color check can be expressed as

$$D_l = \begin{bmatrix} R_{l1}' & G_{l1}' & B_{l1}' \\ R_{l2}' & G_{l2}' & B_{l2}' \\ \cdots & \cdots & \cdots \end{bmatrix}$$

We can obtain the color corrected matrix M_{ccm} as follows (*45*)

$$M_{ccm} = \left(S_l^T S_l\right)^{-1} S_l^T D_l$$

Assuming that the color space of the captured image of the detection zone is O_l, the collected color space O_l' can be obtained by the expression $O_l' = O_l \times M_{\mathrm{ccm}}$.

Custom mobile application design

The custom mobile application was developed using Python. It activates automatically when a QR code on the EE-POCT device is scanned. Users enter their personal information and then use the interface's capture button to take a picture of test zones. The application processes this image using the colorimetric analysis algorithm to measure nine liver-related biomarkers. Results can be saved as a historical record and sent to a physician for diagnosis and treatment. A demonstration of the application's operation is available in movie S11.

Preparation for marker linearity test

The preparation for marker linearity test is provided in fig. S9. For ALB, TP, and Cl^-, 200 μl of Bromo-cresol green solution, 200-μl mixtures of copper sulfate and sodium hydroxide solutions (1:2 ratio), and 120 μl of mercuric thiocyanate solution were added to reagent prestorage chamber #1, respectively. For ALP, 40 μl of DPP solutions was added to chamber #1 and 120-μl mixtures of 4-aminoantipyrine, PF, and sodium hydroxide solutions (1:1:1 ratio) were added to chamber #2. For chamber #2 and #3 of AST and ALT, 25 μl of DNPH solution and 125 μl of sodium hydroxide solution were added, while for their chamber #1, 25-μl mixtures of aspartic acid and α-ketoglutaric acid solutions (1:1 ratio) for AST and 25 μl of alanine solution and α-ketoglutaric acid solution (1:1 ratio) for ALT were added. After adding the reagents, a pressurized gas with a pressure of 65 kPa was inflated into the chamber and the device is ready to use. Before doing the linearity test, 20 μl of known amounts of purified markers to artificial blood serum buffer was added to the sample chamber. The lower LOD was calculated from the sum of the mean signal and threefold SD obtained from the 20-fold blank sample measurements.

All-in-one EE-POCT platform configurations

Two hundred–microliter mixtures of copper sulfate and sodium hydroxide solutions (1:2 ratio); 25 μl of aspartic acid and α-ketoglutaric acid solutions (1:1 ratio); 25 μl of DNPH solution; 125 μl of sodium hydroxide solution; 200 μl of Bromo-cresol green solution; 40 μl of DPP solution; 120-μl mixtures of 4-aminoantipyrine, PF, and sodium hydroxide solutions (1:1:1 ratio); 25 μl of alanine solution and α-ketoglutaric acid solution (1:1 ratio); 25 μl of DNPH solution; 125 μl of sodium hydroxide solution; and 120 μl of mercuric thiocyanate solution were added to chamber #2 to #12, respectively. A pressurized gas with a pressure of 65 kPa was inflated. The lever length of all the levers is 10 mm and the λ values for chamber #2 to #12 are 0.5, 0.5, 3.5, 3.7, 0.5, 0.5, 0.8, 0.5, 3.5, 3.7, and 0.5, respectively. The detailed schematic diagram is provided in fig. S11.

Statistical analysis

All testing results are presented as means ± SD after repeating at least three times using separate EE-POCT platforms with biologically independent samples unless otherwise specified. No data were excluded from the analyses. The experiments were not randomized. The investigator was not blinded to group allocation during the experiment.

Supplementary Materials

The PDF file includes:

Supplementary Text
Figs. S1 to S12
Tables S1 and S2
Legends for movies S1 to S11

Other Supplementary Material for this manuscript includes the following:

Movies S1 to S11

REFERENCES AND NOTES

1. B. Gao, W.-I. Jeong, Z. Tian, Liver: An organ with predominant innate immunity. *Hepatology* **47**, 729–736 (2007).
2. N. Chalasani, Z. Younossi, J. E. Lavine, A. M. Diehl, E. M. Brunt, K. Cusi, M. Charltion, A. J. Sanyal, American Gastroenterological Association, American Association for the Study of Liver Diseases, American College of Gastroenterologyh, The diagnosis and management of non-alcoholic fatty liver disease: Practice guideline by the American Gastroenterological Association, American Association for the Study of Liver Diseases, and American College of Gastroenterology. *Gastroenterology* **142**, 1592–1609 (2012).
3. S. Xin, J. Xu, Y. Yu, Abnormal liver function tests of patients with Coronavirus disease 2019 in mainland China: A systematic review and meta- analysis. *J. Gastrointestin. Liver Dis.* **29**, 219–226 (2020).
4. Q. Cai, D. Huang, H. Yu, Z. Zhu, Z. Xia, Y. Su, Z. Li, G. Zhou, J. Gou, J. Qu, Y. Sun, Y. Liu, Q. He, J. Chen, L. Liu, L. Xu, COVID-19: Abnormal liver function tests. *J. Hepatol.* **73**, 566–574 (2020).
5. H. Devarbhavi, S. K. Asrani, J. P. Arab, Y. A. Nartey, E. Pose, P. S. Kamath, Global burden of liver disease: 2023 update. *J. Hepatol.* **79**, 516–537 (2023).
6. J. Julien, T. Ayer, E. D. Bethea, E. B. Tapper, J. Chhatwal, Projected prevalence and mortality associated with alcohol-related liver disease in the USA, 2019–40: A modelling study. *Lancet Public Health* **5**, e316–e323 (2020).
7. D. G. Le Couteur, F. M. Blyth, H. M. Creasey, D. J. Handelsman, V. Naganathan, P. N. Sambrook, M. J. Seibel, L. M. Waite, R. G. Cumming, The association of alanine transaminase with aging, frailty, and mortality. *J. Gerontol. A Biol. Sci. Med. Sci.* **65**, 712–717 (2010).
8. M. R. McGill, The past and present of serum aminotransferases and the future of liver injury biomarkers. *EXCLI J.* **15**, 1611–2156 (2016).
9. B. R. Thapa, A. Walia, Liver function tests and their interpretation. *Indian J. Pediatr.* **74**, 663–671 (2007).
10. K. M. Choi, K. Han, S. Park, H. S. Chung, N. H. Kim, H. J. Yoo, J.-A. Seo, S. G. Kim, N. H. Kim, S. H. Baik, Y. G. Park, S. M. Kim, Implication of liver enzymes on incident cardiovascular diseases and mortality: A nationwide population-based cohort study. *Sci. Rep.* **8**, 3764 (2018).
11. S. Sepanlou, S. Safiri, C. Bisignano, K. Ikuta, A. Renzaho, The global, regional, and national burden of cirrhosis by cause in 195 countries and territories, 1990–2017: A systematic analysis for the global burden of disease study 2017. *Lancet Gastroenterol. Hepatol.* **5**, 245–266 (2020).
12. W. Siangproh, W. Dungchai, P. Rattanarat, O. Chailapakul, Nanoparticle-based electrochemical detection in conventional and miniaturized systems and their bioanalytical applications: A review. *Anal. Chim. Acta* **690**, 10–25 (2011).
13. M. Santhosh, S. R. Chinnadayyala, A. Kakoti, P. Goswami, Selective and sensitive detection of free bilirubin in blood serum using human serum albumin stabilized gold nanoclusters as fluorometric and colorimetric probe. *Biosens. Bioelectron.* **59**, 370–376 (2014).
14. A. Lakshmi Devi, P. E. Resmi, A. Pradeep, P. V. Suneesh, B. G. Nair, T. G. Satheesh Babu, A paper-based point-of-care testing device for the colourimetric estimation of bilirubin in blood sample. *Spectrochim. Acta A Mol. Biomol. Spectrosc.* **287**, 122045 (2023).

15. A. Koh, D. Kang, Y. Xue, S. Lee, R. M. Pielak, J. Kim, T. Hwang, S. Min, A. Banks, P. Bastien, M. C. Manco, L. Wang, K. R. Ammann, K.-I. Jang, P. Won, S. Han, R. Ghaffari, U. Paik, M. J. Slepian, G. Balooch, Y. Huang, J. A. Rogers, A soft, wearable microfluidic device for the capture, storage, and colorimetric sensing of sweat. *Sci. Transl. Med.* **8**, 366ra165 (2016).
16. Z. Wang, Y. Dong, X. Sui, X. Shao, K. Li, H. Zhang, Z. Xu, D. Zhang, An artificial intelligence-assisted microfluidic colorimetric wearable sensor system for monitoring of key tear biomarkers. *npj Flex. Electron.* **8**, 35 (2024).
17. Y. Tong, Y. Zeng, Y. Lu, Y. Huang, Z. Jin, Z. Wang, Y. Wang, X. Zang, L. Chang, W. Mu, X. Xue, Z. Dong, Deep learning-enhanced microwell array biochip for rapid and precise quantification of *Cryptococcus* subtypes. *View* **5**, 20240032 (2024).
18. E. M. Fenton, M. R. Mascarenas, G. P. López, S. S. Sibbett, Multiplex lateral-flow test strips fabricated by two-dimensional shaping. *ACS Appl. Mater. Interfaces* **1**, 124–129 (2009).
19. K. M. Schilling, A. L. Lepore, J. A. Kurian, A. W. Martinez, Fully enclosed microfluidic paper-based analytical devices. *Anal. Chem.* **84**, 1579–1585 (2012).
20. N. R. Pollock, J. P. Rolland, S. Kumar, P. D. Beattie, S. Jain, F. Noubary, V. L. Wong, R. A. Pohlmann, U. S. Ryan, G. M. Whitesides, A paper-based multiplexed transaminase test for low-cost, point-of-care liver function testing. *Sci. Transl. Med.* **4**, 152ra129 (2012).
21. M. J. Rogers, D. P. McManus, S. Muhi, C. A. Gordon, Membrane technology for rapid point-of-care diagnostics for parasitic neglected tropical diseases. *Clin. Microbiol. Rev.* **34**, e0032920 (2021).
22. E. B. Bahadır, M. K. Sezgintürk, Lateral flow assays: Principles, designs and labels. *TrAC Trends Anal. Chem.* **82**, 286–306 (2016).
23. S. Ahmed, M.-P. N. Bui, A. Abbas, Paper-based chemical and biological sensors: Engineering aspects. *Biosens. Bioelectron.* **77**, 249–263 (2016).
24. M. Yafia, O. Ymbern, A. O. Olanrewaju, A. Parandakh, A. S. Kashani, J. Renault, Z. Jin, G. Kim, A. Ng, D. Juncker, Microfluidic chain reaction of structurally programmed capillary flow events. *Nature* **605**, 464–469 (2022).
25. J. Li, Y. Liu, T. Wu, Z. Xiao, J. Du, H. Liang, C. Zhou, J. Zhou, Barbed arrow-like structure membrane with ultra-high rectification coefficient enables ultra-fast, highly-sensitive lateral-flow assay of cTnI. *Nat. Commun.* **15**, 5603 (2024).
26. K. Tsougeni, D. Papageorgiou, A. Tserepi, E. Gogolides, "Smart" polymeric microfluidics fabricated by plasma processing: Controlled wetting, capillary filling and hydrophobic valving. *Lab Chip* **10**, 462–469 (2010).
27. H. Yuan, C. Wan, X. Wang, S. Li, H. Xie, C. Qian, W. Du, X. Feng, Y. Li, P. Chen, B.-F. Liu, Programmable gravity self-driven microfluidic chip for point-of-care multiplied immunoassays. *Small* **20**, e2310206 (2024).
28. C. Liang, Z. Yang, H. Jiang, A film-lever actuated switch technology for multifunctional, on-demand, and robust manipulation of liquids. *Nat. Commun.* **13**, 4902 (2002).
29. J.-H. Wang, L. Cheng, C.-H. Wang, W.-S. Ling, S.-W. Wang, G.-B. Lee, An integrated chip capable of performing sample pretreatment and nucleic acid amplification for HIV-1 detection. *Biosens. Bioelectron.* **41**, 484–491 (2013).
30. L. Cime, D. Brassard, M. Cerssler, T. Veres, Active pneumatic control of centrifugal microfluidic flows for lab-on-a-chip applications. *Lab Chip* **15**, 2400–2411 (2015).
31. Z. Wang, Y. Wang, L. Lin, T. Wu, Z. Zhao, B. Ying, L. Chang, A finger-driven disposable micro-platform based on isothermal amplification for the application of multiplexed and point-of-care diagnosis of tuberculosis. *Biosens. Bioelectron.* **195**, 113663 (2022).
32. J. Park, D. H. Han, S.-H. Hwang, J.-K. Park, Reciprocating flow-assisted nucleic acid purification using a finger-actuated microfluidic device. *Lab Chip* **20**, 3346–3353 (2020).
33. B. Utzinger, D. D. Dixit, P. B. Lillehoj, Microfluidic finger-actuated mixer for ultrasensitive electrochemical measurements of protein biomarkers for point-of-care testing. *Lab Chip* **24**, 3802–3809 (2024).
34. World Health Organization. *Global Prevalence and Incidence of Selected Curable Sexually Transmitted Infections: Overview and Estimates* (WHO, 2001).
35. S. Skullman, M. Wirén, P. J. Garlick, M. A. McNurlan, J. Larsson, Protein synthesis in regenerating rat liver during malnutrition. *J. Hepatol.* **21**, 174–181 (1994).
36. J. V. Jiménez, D. L. Carrillo-Pérez, R. Rosado-Canto, I. García-Juárez, A. Torre, D. Kershenobich, E. Carrillo-Maravilla, Electrolyte and acid–base disturbances in end-stage liver disease: A physiopathological approach. *Dig. Dis. Sci.* **62**, 1855–1871 (2017).
37. T. J. G. Gevers, F. Nevens, V. E. Torres, M. C. Hogan, J. P. H. Drenth, Alkaline phosphatase predicts response in polycystic liver disease during somatostatin analogue therapy: A pooled analysis. *Liver Int.* **36**, 595–602 (2016).
38. F. A. Rochling, Evaluation of abnormal liver tests. *Clin. Oncol.* **3**, 1–12 (2001).
39. G. J. Park, B. P. Lin, M. C. Ngu, D. B. Jones, P. H. Katelaris, Aspartate aminotransferase: Alanine aminotransferase ratio in chronic hepatitis C infection: Is it a useful predictor of cirrhosis? *J. Gastroenterol. Hepatol.* **15**, 386–390 (2000).
40. S. F. Friedman, P. Martin, J. S. Munoz. *Laboratory Evaluation of the Patient with Liver Disease. Hepatology, a Textbook of Liver Disease* (Saunders Publication, 2003).
41. Y. Wang, B. B. Nunna, N. Talukder, E. E. Etienne, E. S. Lee, Blood plasma self-separation technologies during the self-driven flow in microfluidic platforms. *Bioengineering.* **8**, 94 (2021).
42. X. Chen, T. Li, H. Zeng, Z. Hu, B. Fu, Numerical and experimental investigation on micromixers with serpentine microchannels. *Int. J. Heat Mass Transf.* **98**, 131–140 (2016).
43. A. D. Stroock, S. K. W. Dertinger, A. Ajdari, I. Mezić, H. A. Stone, G. M. Whitesides, Chaotic mixer for microchannels. *Science* **295**, 647–651 (2002).
44. M. Grumann, A. Geipel, L. Riegger, R. Zengerle, J. Ducrée, Batch-mode mixing on centrifugal microfluidic platforms. *Lab Chip* **5**, 560–565 (2005).
45. R. Zhao, J. Wang, G. B. Yu, J. Zhong, W. Zhou, Y. Li, "A method of color correction of camera based on HSV model," in *7th International Symposium on Advanced Optical Manufacturing and Testing Technologies: Optoelectronics Materials and Devices for Sensing and Imaging* (SPIE, 2014). Vol. 9284.
46. M. Astegiano, N. Sapone, B. Demarchi, S. Rossetti, R. Bonardi, M. Rizzetto, Laboratory evaluation of the patient with liver disease. *Eur. Rev. Med. Pharmacol. Sci.* **8**, 3–9 (2004).
47. F. Ellett, J. Jorgensen, A. L. Marand, Y. M. Liu, M. M. Martinez, V. Sein, K. L. Butler, J. Lee, D. Irimia, Diagnosis of sepsis from a drop of blood by measurement of spontaneous neutrophil motility in a microfluidic assay. *Nat. Biomed. Eng.* **2**, 207–214 (2018).
48. W. Zheng, S. M. LaCourse, B. Song, D. K. Singh, M. Khanna, J. Olivo, J. Stern, J. N. Escudero, C. Vergara, F. Zhang, S. Li, S. Wang, L. M. Cranmer, Z. Huang, C. M. Bojanowski, D. Bao, I. Njuguna, Y. Xiao, D. C. Wamalwa, D. T. Nguyen, L. Yang, E. Maleche-Obimbo, N. Nguyen, L. Zhang, H. Phan, J. Fan, B. Ning, C. Li, C. J. Lyon, E. A. Graviss, G. John-Stewart, C. D. Mitchell, A. J. Ramsay, D. Kaushal, R. Liang, E. Pérez-Then, T. Y. Hu, Diagnosis of paediatric tuberculosis by optically detecting two virulence factors on extracellular vesicles in blood samples. *Nat. Biomed. Eng.* **6**, 979–991 (2022).
49. H. Im, D. Pathania, P. J. McFarland, A. R. Sohani, I. Degani, M. Allen, B. Coble, A. Kilcoyne, S. Hong, L. Rohrer, J. S. Abramson, S. Dryden-Peterson, L. Fexon, M. Pivovarov, B. Chabner, H. Lee, C. M. Castro, R. Weissleder, Design and clinical validation of a point-of-care device for the diagnosis of lymphoma via contrast-enhanced microholography and machine learning. *Nat. Biomed. Eng.* **2**, 666–674 (2018).
50. I. Michael, D. Kim, O. Gulenko, S. Kumar, S. Kumar, J. Clara, D. Y. Ki, J. Park, H. Y. Jeong, T. S. Kim, S. Kwon, Y.-K. Cho, A fidget spinner for the point-of-care diagnosis of urinary tract infection. *Nat. Biomed. Eng.* **4**, 591–600 (2020).
51. D. Wang, S. He, X. Wang, Y. Yan, J. Liu, S. Wu, S. Liu, Y. Lei, M. Chen, L. Li, J. Zhang, L. Zhang, X. Hu, X. Zheng, J. Bai, Y. Zhang, Y. Zhang, M. Song, Y. Tang, Rapid lateral flow immunoassay for the fluorescence detection of SARS-CoV-2 RNA. *Nat. Biomed. Eng.* **4**, 1150–1158 (2020).
52. C. E. Nwankire, M. Czugala, R. Burger, K. J. Fraser, T. M. O'Connell, T. Glennon, B. E. Onwuliri, I. E. Nduaguibe, D. Diamond, J. Ducrée, A portable centrifugal analyser for liver function screening. *Biosens. Bioelectron.* **56**, 352–358 (2014).

Acknowledgments: We acknowledge the Research Center for Industries of the Future (RCIF) at Westlake University and Westlake Education Foundation for supporting this work. **Funding:** This work was supported by the National Natural Science Foundations of China (grant 12350003) and the Natural Science Foundations of Hangzhou (grant 2024SZRYBH180012). **Author contributions:** Conceptualization: C.L. and H.J. Methodology: C.L., J.Z., P.W., and K.W. Investigation: C.L. and J.Z. Visualization: C.L., J.Z., and K.W. Supervision: H.J. Writing—original draft: C.L. and H.J. Writing—review and editing: C.L., J.Z., P.W., and H.J. **Competing interests:** The authors declare that they have no competing interests. **Data and materials availability:** All data needed to evaluate the conclusions in the paper are present in the paper and/or the Supplementary Materials.

Submitted 24 February 2025
Accepted 7 July 2025
Published 8 August 2025
10.1126/sciadv.adx0092